CHAPTER 6

INFLUENCE OF SMALL Li CONCENTRATION ON LOCAL STRUCTURE, OPTICAL AND MAGNETIC PROPERTIES OF TERBIUM DOPED ZINC OXIDE NANOPARTICLES

6.1. INTRODUCTION

In the previous chapter, we have studied the effect of Li concentration on local structure optical and magnetic properties of Eu doped ZnO. This chapter explains the similar type of study using Tb as dopant ion. The incorporation of rare earth in dilute magnetic semiconductor (DMS) shows promising applications due to the presence of visible luminescent properties combined with special properties of DMS. The large Stokes shift, narrow emission band width and long emission lifetime of rare earth have attracted worldwide attention [170,175]. All rare earth have intense and narrow emission at a specific colour such as Eu exhibit sharp emission in red colour. The partially filled *f*-orbital of rare earth carries magnetic moment, which may take part in magnetic coupling such as transition metals with partially filled *d* orbital. Ferromagnetism in Tb doped ZnO has been reported by different authors [149]. The magnetic properties of zinc oxide doped with different materials are investigated for their possible applications in spintronics devices. The zinc oxide exhibits relatively long room temperature coherence time. It can be *p*-type or *n*-type by selection of appropriate doping [176]. This leads to bipolar spintronics based on ZnO. The ferromagnetism in zinc oxide mediated by both electron and holes has been reported. The presence of RTFM in zinc oxide is quite controversial. DMS involves both charge and spin of the electron for device applications. The optical and magnetic properties of DMS are affected by carrier and mobility of dopant ions.

The large absorption and bright green emission make Tb^{+3} ions a suitable dopant in a host matrix. Terbium doped phosphor materials have been used in three bands fluorescent lamp, x-ray intensifying screen and projection television tubes [177]. *Hastir et al.* reported sensor application of Tb-doped ZnO nanoparticles [178]. They have used different rare earth (Tb, Dy and Er) for gas sensing application and reported that Tb doped ZnO exhibit best sensing response. *Dhlamini et al.* found enhancement of cathode-luminescence (CL) intensity in Tb^{+3} ions doped ZnO-SiO_2 binary system [179]. They have successfully tuned the emitting colour by varying Tb concentrations. The incorporation of rare earth into wide band gap semiconductor leads to a significant change in structural, optical, magnetic and electrical properties. Tb doped ZnO nano-phosphor has been proposed for solid state lighting application [180]. In phosphor converted LED (pc-LED), the blue or ultra-violet emission are converted to light of longer wavelength using phosphor. The intensity of blue, green and other visible emission in ZnO depends on the concentration of different type of defects such as Zn interstitial, Zn vacancy, oxygen interstitial, oxygen vacancy, etc. Therefore, intensity can be tuned by precise control of defect species and their population density for pc-LED. However, it is quite difficult. The desired emission can be obtained by choosing appropriate rare earth dopant. The Tb doped ZnO with different morphology such as microsphere, nanotube, nanorod, nanowires and nanocones have been reported earlier [181]. The large ionic radius mismatch between Tb^{+3}(0.92Å) and Zn^{+2}(0.74Å) makes difficult to keep Tb ions at Zn site for a long time [182]. The ionic radius mismatch can expel the impurity out of the ZnO lattice. The accumulation of Tb on the surface of ZnO nanocrystal and Tb nanocluster formation have also been reported [183]. Charge compensation phenomenon in high ionic radius material doped zinc oxide occurs with the help of local defects and small crystal structure deformation. The alkali metals (Na, K, and Li) have been deemed as a promising candidate for charge compensator. The earlier study suggests that Li is most suitable for this purpose. The incorporation of higher Li concentration makes ZnO a *p*-type material. The effect of Li on structural optical and magnetic properties has been studied [150]. Li doped ZnO exhibit efficient multicoloured emission and studied for organic light diode application[184]. The ferromagnetism in Li-doped zinc oxide has been obtained by *Awan et al.*[151]. The presence of Li at interstitial and substitutional position depends on concentration. The theoretical study on Li doped ZnO has been done by several groups. *Park et al.* found ionisation energy of Li substitutional is 90meV and suggest that *p*-type doping efficiency of Li is limited [185].

In this study, we have investigated the role of different Li concentration (0.25-1.0%) on local structure, optical and magnetic properties of Tb (1%) doped ZnO nanoparticles. The local structure of sol-gel derived samples has been studied with the help of X-ray absorption spectroscopy (XAS) analysis. We found absorption edge shifted towards the visible region, luminescence property enhances significantly by the small amount of Li concentration and magnetic behaviour changes by Tb doping. This study firmly empowers the investigation on local structure, luminescence and magnetic properties of (Tb, Li) doped ZnO. The observed enhanced luminescence may be useful in the Tb doped ZnO based optical devices.

6.2. EXPERIMENTAL PROCEDURE

6.2.1 Synthesis of Nanoparticles

The Tb, Li co-doped ZnO nanoparticles have been synthesized by the simple sol-gel method using high purity analytical grade acetates of zinc, terbium and lithium. We have prepared pure zinc oxide, Tb (1%) doped zinc oxide and Tb (1%) doped zinc oxide co-doped with different lithium concentration (0.25%, 0.5% and 1.0%). The compositions are indicated with code name ZnO, Tb1, Li0.25, Li0.5 and Li1.0 respectively. Briefly, for Tb (1%) doped ZnO preparation, we take the stoichiometric amount of zinc acetate dehydrate and dissolve it into isopropyl alcohol with magnetic stirring for 1h. After that, stoichiometric amount of terbium (iii) acetate hydrate was added, and stirring continues 2h for complete dissolution of the precursor. Urea has been added for proper burning and the resultant solution was stirred till the formation of the gel. During the complete process, the temperature and rpm were maintained at 80^0C and 1200 rpm respectively. The obtained gel was burnt at 500^0C for 30 min. Further, it was sintered at 600^0C for 2h in pellet form for proper crystallisation and to remove the impurities of samples. For characterisation purpose, we used powder samples obtained by crushed pellets.

6.2.2 Characterisations

The phase formation of synthesized samples have been confirmed using Rigaku-MiniFlex-II DESKTOP powder X-ray diffractometer with CuK_α radiation (λ= 1.54 Å) at 30 kV and 15mA. We have recorded the diffraction patterns over the range $20^0 \leq 2\theta \leq 90^0$ with a step size of 0.02º. Thermal analysis has been carried out by METTLER TOLEDO Japan in the presence of nitrogen. The morphology and particle sizes of samples have been investigated with TEM analysis using TECNAI G^2 200kV (FEI) Transmission Electron Microscope. The presence of all elements in samples is confirmed by OXFORD Instrument SEM EVO 18 Research. X-ray photoemission spectroscopy (XPS) experiments were carried out using an Omicron Multiprobe Surface Science System, equipped with a dual anode non-monochromatic Mg/Al X-ray source (DAR400) and a hemispherical electron energy analyzer (EA 125). Throughout, the photoemission experiments were carried out at an average base pressure of 2.25×10^{-10} Torr with a power of 300 W. The total energy resolution, estimated from the width of the Fermi edge, was about 0.7 eV for the non-monochromatic MgKα line with the photon energy of 1253.6 eV. The pass energy for survey scan spectra and core level spectra was kept at 50 eV and 30 eV, respectively. Ar-ion sputtering was performed at 2 keV by maintaining an extractor pressure of 25±0.3 mPa. During the sputtering average vacuum maintained to

1.75×10^{-8} Torr. LABRAM-HR dispersive Raman spectrometer has been used to collect Raman spectra ranging from 100 to 1300 cm^{-1}. The optical absorption spectra of the samples have been recorded with the help of JASCO V750 UV-Vis spectrophotometer in the range of 200nm-800nm. The photoluminescence study has been carried out by Horiba Fluorolog-3 spectrophotometer equipped with 450w xenon flash lamp. Fourier transforms infrared (FTIR-8400S) spectrophotometer has been employed to collect information about functional groups present in the samples. The magnetic measurements have been done using Quantum Design MPMS-3 magnetometer in temperature range 5-300 K. The investigation of the local structure has been carried out at Raja Ramanna Centre for Advanced Technology (RRCAT), Indore, India, with the Energy-Scanning EXAFS beamline (BL-9) in fluorescence mode at the Indus-2 Synchrotron Source (2.5GeV, 200mA).

6.3. RESULTS AND DISCUSSIONS

6.3.1 Thermal Analysis

Figure 6.1 depicts the Thermo gravimetric analysis (TGA)-Differential scanning calorimetry (DSC) curves of Tb (1%) doped ZnO. The thermal property has been analysed using sample burnt at 500^0C for 30 min. The characterization has been carried out in the nitrogen atmosphere with the rate of 10^0C/min. The TGA graphs show that major weight loss (24%) has been taking place within temperature range 485^0C-652^0C in a single step. However, The DSC curve exhibits two exothermic peaks at 597^0C and 630^0C, which are attributed to the burning of fuel and reaction among the reactants respectively. The maximum weight loss occurs in the region of exothermic peaks; similar behaviour has also been obtained by *Guo et al.*[186]. The TGA curves have no remarkable change after 650^0C. Nearly constant curve of TGA after 650^0C indicate the formation of Tb (1%) doped ZnO nanoparticles as the decomposition product. Since the crystallisation process depends on temperature as well as the time duration of heating. Thus, we anneal the sample at 600^0C for 2 hrs to get the crystalline sample.

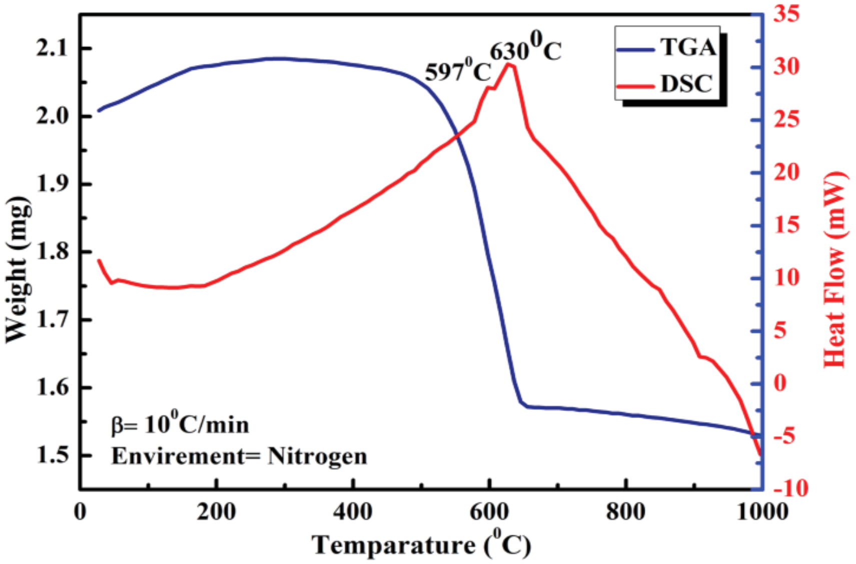

Figure 6.1: TGA- DSC of ZnO:Tb(1%) nanoparticles.

6.3.2. Structural Analysis

The rietveld refined x-ray diffraction spectra of pure and doped ZnO nanoparticles sintered at 600^0C are shown in Figure 6.2. The observed XRD patterns are very close to standard Bragg's position of hexagonal wurtzite crystal of zinc oxide (PDF: 792205). The XRD spectra exhibit sharp and intense peaks; this indicates crystalline nature of the samples. All XRD diffraction peaks have been assigned unambiguously to the standard peak position of wurtzite zinc oxide. The prominent peaks of ZnO are also present in doped zinc oxide samples without any addition impurity phase, which confirms that all samples have the same crystal structure and belongs to $P6_3mc$ space group. The absence of terbium oxides related peak indicates that Tb present as a substitutional dopant in zinc oxide. The Scherer's formula has been employed to estimate crystallite size of all samples under investigation (Equation 3.1). The calculated values of crystallite size are listed in Table 6.1. It can be pointed out that crystallite size decreases due to Tb doping. The incorporation of Li results an increase in crystallite size. The growth of ZnO grains is controlled by moment and diffusion of Zn^{+2} ions and this affects the crystallite size. The presence of Tb in the lattice restrains the grain growth and causes decreases in crystallite size. The decrease in crystallite size due to Tb doping has also been reported by *Pal et al.*[152]. The incorporation of Li in the host increases its electrical conductivity due increase in number of conducting electrons in the system and favours the grain growth. Thus the crystallite size increases with Li concentration. The rietveld refinement of all samples has been carried out to obtain the lattice parameters of the samples. The values of lattice parameters and Rietveld refinement fitting parameters are listed in Table 6.1. We found that lattice parameters increase due to Tb doping in ZnO. The ionic radius of Tb^{+3} (0.92Å) is larger than Zn^{+2}(0.74Å) [182]. Therefore, substitution of Tb^{+3} at Zn^{+2} site causes lattice expansion and increases lattice parameters. The Li^{+} ions (0.6Å) have the small ionic radius as compare to Zn^{+2}(0.74Å). The Li^{+} ions can easily incorporate into the system and take an interstitial position. The occurrence of Li in interstitial position support lattice expansion. Therefore, lattice parameters a and c increases for Li0.25. Further increase in Li concentration causes substitution of Li^{+} at Zn^{+2} site of ZnO crystal structure. The presence of Li at substitutional position indicates a small decrease in lattice parameters (Table 6.1). The ratio of lattice parameter for ideal HCP structure is, c/a=1.633. The calculated value of c/a=1.60 and a small decrease in value has been obtained with dopant concentration. This indicates an increase in lattice distortion and shift of crystal structure towards higher symmetry. The unit cell volume has been estimated using Equation 4.1. The values of the unit cell are listed in Table 6.1. The variation can be attributed to change in lattice parameters. Atomic packing fraction (APF) has been calculated using Equation 4.2. The values of APF are listed in Table 6.1. The APF value of bulk ZnO is 74%, while in our case calculated value is approximately 75%.The slight variation in APF can be attributed to size effect of nanoparticles. It can be pointed out that APF values are continuously increasing with dopant concentration. This variation indicates that system is more closely packed due to the presence of dopant.

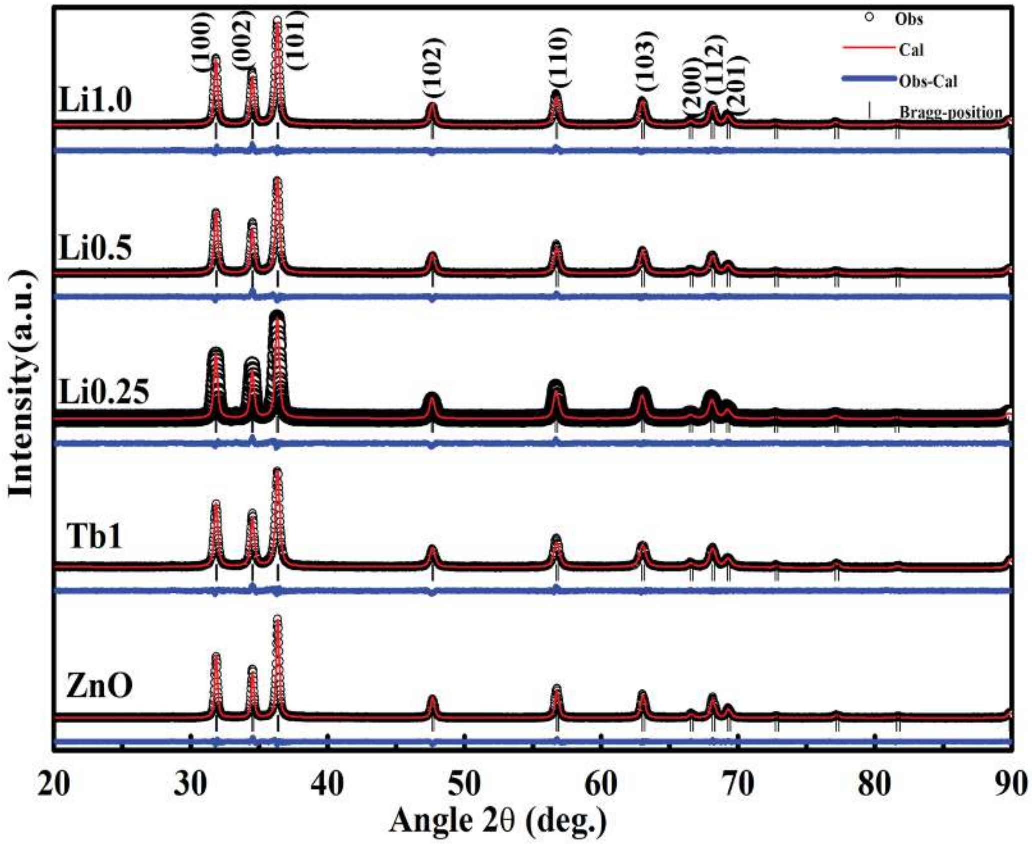

Figure 6.2: Rietveld refine XRD patterns of pure and doped zinc oxide nanoparticles.

Table 6.1. The lattice parameters, crystallite size, cell volume, atomic packing fraction and Rietveld refinement fitting parameters of the samples.

Sample Code name	Lattice parameter		Ave. crystallite size(nm)	Cell volume $(Å)^3$	APF	R_p	R_{wp}	R_{exp}	χ^2
	a(Å)	c(Å)							
Zn	3.24294(14)	5.19595(13)	27.3	47.323	0.75503	9.08	11.2	5.12	3.73
Tb1	3.24438(18)	5.1972(3)	23.4	47.377	0.75512	10.2	11.7	4.92	3.68
Li0.25	3.24606(14)	5.19990(20)	24	47.45	0.75515	10.9	12.3	5.59	4.86
Li0.5	3.24467(14)	5.19750(20)	24.9	47.387	0.7552	10.9	12.1	5.52	3.80
Li1.0	3.24553(13)	5.19890(20)	25.9	47.426	0.7552	10.6	12.2	5.39	3.12

6.3.3. Morphology and Elemental Analysis

The morphology and particle size of the samples have been deliberated by Transmission electron microscopy (TEM) analysis. The elemental analysis has been carried out with Energy dispersive X-ray spectroscopy (EDS) to ascertain the presence of all elements in the samples. TEM image of ZnO, Tb1 and Li1.0 are shown in Figure 6.3(a), (b) and (c) respectively. It can be pointed out that all samples exhibit approximately spherical shape and smooth surface. The incorporation of dopant affects the particle size but it could not make any significant change in morphology of samples. The TEM image indicates that particles are stuck together and looks like a cluster. This may be due to an artefact of drying on an aqueous suspension or effect of electrostatic force. The particle size distribution shown in the inset of Figure 6.3(a), (b) and (c) confirms that most of the particles lie in the range of 50nm-60nm for pure ZnO, 40nm-50nm for Tb1 and 40nm-50nm for Li1.0. The average particle size has been calculated considering a large number of particles. It has been found that average particle size for pure ZnO, Tb1 and Li1.0 are 60nm, 42nm and 46nm respectively. Selected area electron diffraction (SAED) pattern of Tb1 is shown in Figure 6.3(d). The ring pattern ascertains the polycrystalline nature of samples. ZnO and Li1.0 also have a similar type of diffraction pattern. The qualitative and quantitative analysis of ZnO and Tb1 has been performed. Figure 6.4 shows the EDS spectra and elemental mapping of Tb1. The EDS analysis indicates distribution and relative proportion of the elements in the scanned area. The pie chart delineates the existence of all elements in appropriate proportion. The instrument used for EDS could not identify the presence of Li due to the detection limit. Further, XPS analysis has been carried out to confirm the presence of Li.

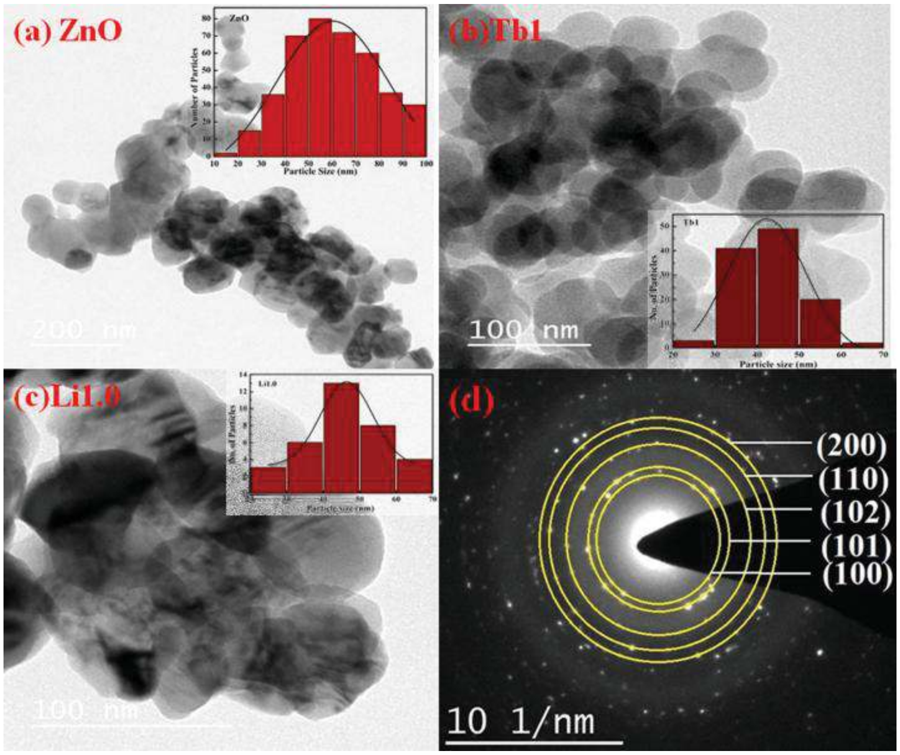

Figure 6.3: TEM image and particle size distribution of **(a)** ZnO **(b)** ZnO:Tb(1%) **(c)** ZnO:Tb(1%):Li(1%) nanoparticles. **(d)** SAED pattern of ZnO:Tb(1%) nanoparticles.

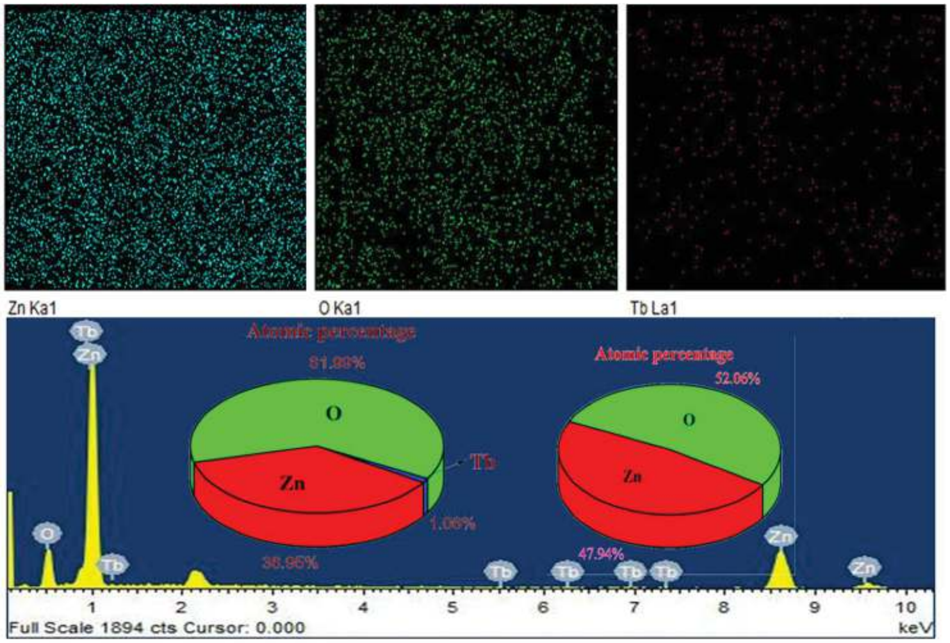

Figure 6.4: EDS spectra, elemental mapping of ZnO:Tb and atomic percentage distribution of ZnO and ZnO:Tb nanoparticles.

6.3.4 FTIR Analysis

The functional groups present in the samples have been identified by analysing absorption of electromagnetic waves at different frequencies. The room temperature Fourier transform infrared spectroscopy (FTIR) spectra of all samples have been recorded within the wave number range of 400-4000 cm^{-1} and shown in Figure 6.5. There is no significant change in peak positions of ZnO sample due to doping of Tb and Li. The absorption bands of metal oxides arise due to inter-atomic vibrations and lie in the fingerprint region (i.e. below 1000 cm^{-1}) [187]. The vibrational frequencies observed at 605 cm^{-1} in pure ZnO and 595 cm^{-1} in doped ZnO can be assigned as Zn-O stretching mode, while the peak at 862 cm^{-1} represents weak vibration of Zn-O. The small shift in the wave number is due to the atomic mass difference between Zn and Tb ions [188]. The observed stretching modes of Zn-O bonds confirm the wurtzite structure formation of all the samples. The peaks near 1408 cm^{-1} and 1514 cm^{-1} indicate symmetric and asymmetric stretching of C=O group, which may be due to zinc acetate used in the reaction. The peaks around 990 cm^{-1} represents the O-H asymmetric stretching, while the peak at 1910 cm^{-1} can be attributed to carbonyl ligands [52]. The vibrational frequencies observed at 2348 cm^{-1} indicate presence of CO_2 molecule. It may be possible that sample has trapped some CO_2 molecule from the atmosphere. The presence of hydroxide group in all samples has been ascertained by spanning peak around 3400 cm^{-1}. This observed O-H bond can be attributed to reversible dissociative absorption of hydrogen on Zn as well as O site [187]. The presence of vibrational frequencies at approximately same wave number and absence of extra peaks in doped ZnO nanoparticles, confirms that all samples retained their hexagonal wurtzite crystal structure.

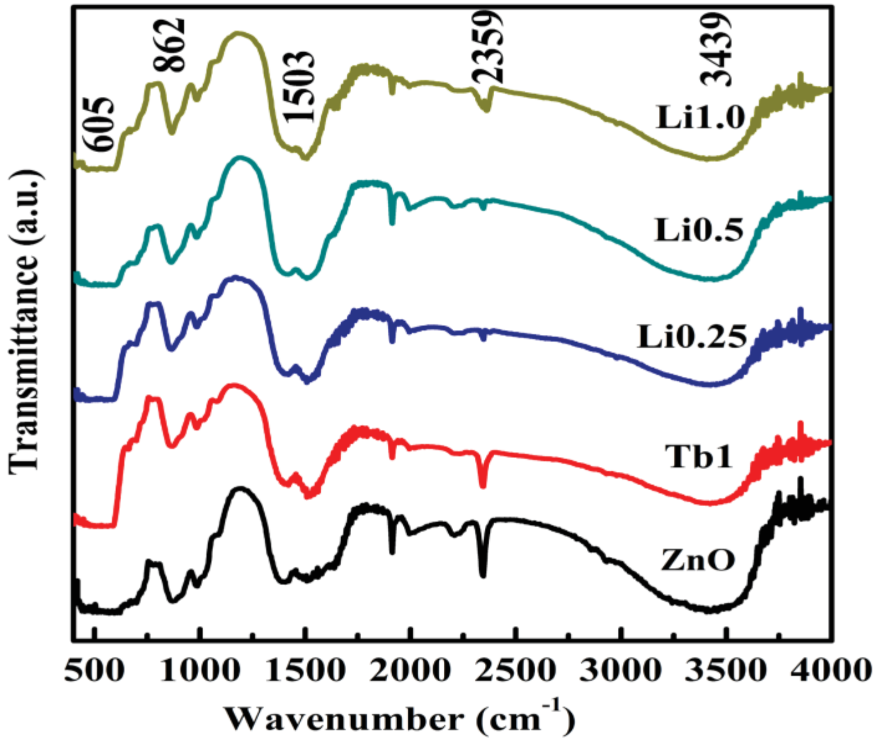

Figure 6.5: FTIR spectra of pure and doped zinc oxide nanoparticles.

6.3.5 Raman Analysis

The Raman analysis has been carried out to investigate the influence of dopant on vibrational properties, defect, and lattice disorder of zinc oxide. Raman spectroscopy ascertains the crystalline quality by the change in wave numbers. Wurtzite ZnO exhibit 12 phonon modes, these modes are composed of seven optical [three longitudinal-optical (LO) and four transverse-optical (TO)] and three acoustic [one longitudinal-acoustic (LA) two transverse-acoustic (TA)]. The optical phonons irreducible representation is mentioned in previous chapter (Equation 4.3). The Raman active E_2 mode consists of two parts, namely E_2^{low} and E_2^{high}, which are associated with the motion of zinc sub-lattice and oxygen respectively. The room temperature Raman spectra of pure and doped ZnO samples in the range of 50-1300 cm^{-1} are shown in Figure 6.6(a). The first mode observed around 103 cm^{-1} shows a slight shift towards lower wave number with Tb doping. Figure 6.6(b) shows the shift in E_2^{low} peak position. The shift toward lower wavelength with Tb doping has also been observed by *Hastir et al.*[189]. The wavelength shifts are affected by size of particles. At nanometre scale, the phenomenon can be explained with the help of phonon confinement model [190]. The doping of materials results change in lattice periodicity, which causes relaxation in selection rule. The phonon relaxed with selection rules are also involve in Raman scattering process and indicates shift or broadening of Raman peaks. The incorporation of small lithium concentration (Li0.25%) in Tb (1%) doped ZnO shows the peak at a same position as host due to charge compensation [Figure 6.6(b)]. This indicates a decrease in lattice defects. The increase in Li concentration causes substitution of Li at Zn site, which enhances the lattice defect and shift the peak towards lower wavelength. The decrease in intensity indicates structural disorder and loss of crystalline structure. The Raman study clearly indicates the effect of dopant and presence of prominent peaks of ZnO in all the samples confirms that samples preserve the same crystal structure.

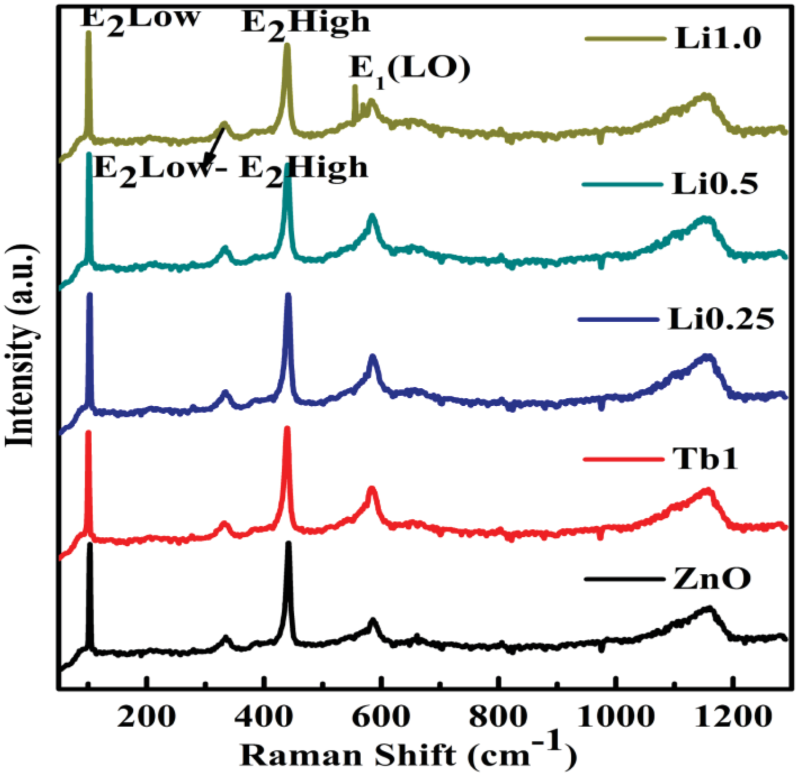

Figure 6.6(a): Raman spectra of pure and doped zinc oxide.

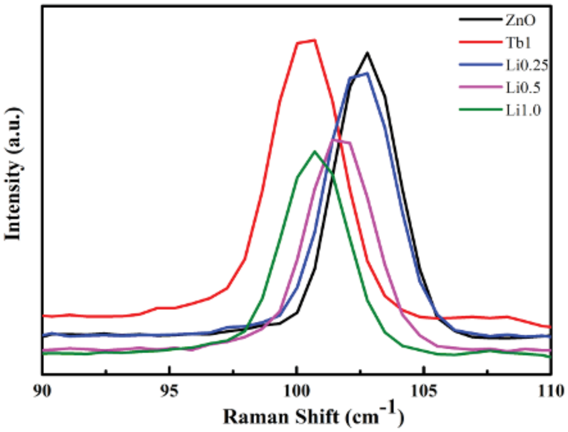

Figure 6.6(b): Intensity variation of E_2 Low in Raman spectra of pure and doped ZnO.

6.3.6 XPS Analysis

The X-ray photoelectron spectrum (XPS) analysis has been carried out to obtain information about oxidation state and presence of atom at different positions (substitutional/interstitial). The position of an element affects the optical and magnetic properties of the system. We have carried out XPS analysis of three samples namely, ZnO, Tb1 and Li1.0. The XPS survey shown in Figure 6.7(a) indicates that all prominent peaks of Zn, O and C are present in the samples. A charging effect observed which were calibrated using the binding energy of C1s peak at 284.6eV. The XPS spectra for individual elements are plotted to determine the chemical oxidation state of Zn, Tb, O and Li. The presence of carbon peak in the samples is due to atmospheric carbon adsorb on the surface of samples. The XPS spectra of Zn 2p core level are shown in Figure 6.7(b). The XPS spectra of pure ZnO contains two peaks at 1047eV and 1024eV corresponding to $2p_{1/2}$ and $2p_{3/2}$ respectively [151]. The presence of Tb in sample affects the peak position of Zn 2p core level XPS spectra. The peaks in Tb1 sample are observed at 1045eV and 1022eV for $2p_{1/2}$ and $2p_{3/2}$ respectively, due to spin-orbit splitting. The slight variation in peaks of Zn doublet indicates substitution of Tb at Zn^{+2} site of ZnO crystal structure [178]. The binding energy shift can be attributed to charge redistribution in the process of chemical interaction. The shift in the binding energy confirms the electronic interaction between host and dopant. The observed slight variation in binding energy indicates partial replacement of lattice Zn ions by Tb in Tb doped ZnO lattice forming Zn-O-Tb bonds. The observed difference of two strong peaks of Zn 2p core level is approximately 23eV, which suggest that zinc is present in +2 oxidation state [178]. It has been observed that Zn 2p peaks tend toward its original position with Li co-doping in the sample. The Zn doublet peaks in Li1.0 are observed at 1046.8eV and 1023.7eV correspond to $2p_{1/2}$ and $2p_{3/2}$ respectively with 23.1eV difference. It is worth mentioned that for pure ZnO spin-orbit splitting may be observed at 23eV while for elemental Zn it occurred at 23.1eV. Therefore, Li may affect valence state of Zn. The observed variation in binding energy may be attributed to the formation of Li-O and Zn-O-Li bonds. In addition, the presence of Tb^{+3} ions affects the local environment around Zn ions and creates disorder in the system; as a result, Zn peaks shift from its original position. The lattice disorder decreases with charge compensation phenomenon due to Li co-doping. The EXAFS study at Tb L3 edge (Figure 6.15) indicates that disorder factor and coordination number around Tb edge is reduced due to Li co-doping. Therefore, the effect of Tb^{+3} ions on lattice distortion of the system reduces and lattice tends towards pure ZnO crystal structure. The spectra for Tb 4d spectrum are depicted in Figure 6.7(c). The peak observed at the binding energy 151eV can be attributed to +3 oxidation state of Tb and indicate bond formation due to Tb substitution [191]. A broad Auger peak is also observed at 176.8eV, which is attributed to $M_{4,5}N_{4,5}V$ transition. The shift in the binding energy of Tb^{+3} has been observed due to the presence of Li^{+} ions in the system. The XPS spectra of oxygen 1s peak of all samples are shown in Figure6. 7(d). XPS spectra of O 1s exhibit the strong peak at 532eV and the small peak at 534eV, which is attributed to the presence of OH group at ZnO surface [192]. The observed peak at lower binding energy (532eV) can be interpreted as oxygen ions of Zn-O bonding in hexagonal wurtzite crystal structure of ZnO. The peak at higher binding energy (534eV) indicates defect oxygen or oxygen vacancies [151]. Tb and Li substitution causes a lattice distortion and hence affect the change in the binding energy O (1s) core in ZnO matrix. Figure 6.7(e) indicates XPS core level spectra of Li in the range of 51-57eV confirms the presence of Li at 52.9eV [191]. The small decrease in lattice parameters (Table 6.1) indicates the substitution of Li at Zn site.

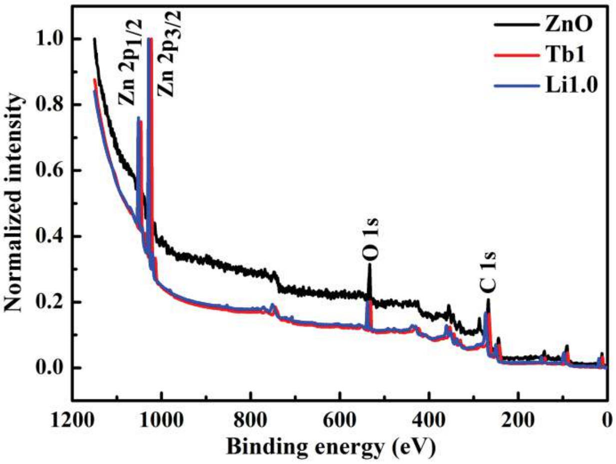

Figure 6.7(a): XPS survey scan spectra of ZnO, Tb1 and Li1.0 nanoparticles.

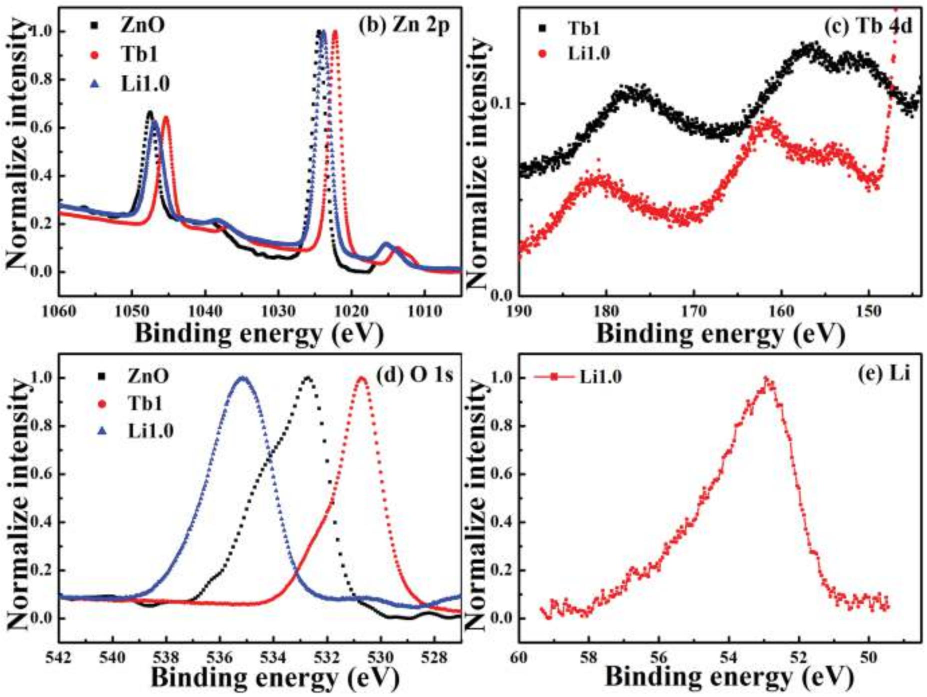

Figure 6.7: XPS Core level spectra of **(b)** Zn (2p) **(c)** Tb (4d) **(d)** O (1s) **(e)** Li (1s).

6.3.7 X-Ray Absorption Spectroscopy (XAS)

XANES Analysis

The Normalized XANES measurements at Zn and Tb edge are shown in Figure 6.8 and Figure 6.9 respectively. The Zn K-edge position matches with ZnO indicates that Zn is present in +2 oxidation state in Tb doped and Tb, Li co-doped ZnO. The Tb L3 edge XANES measurements shown in Figure 6.9 indicate that the local environment of Tb-doped ZnO and Tb, Li co-doped ZnO is same. A small change in Li1.0 has been observed near 7526eV. XANES measurement confirms that Tb ions are doped in ZnO as Tb^{+3} [59-60], and this also exclude the possibility of another phase of Tb. The XRD, Raman and FTIR results also indicate the absence of impurity phases.

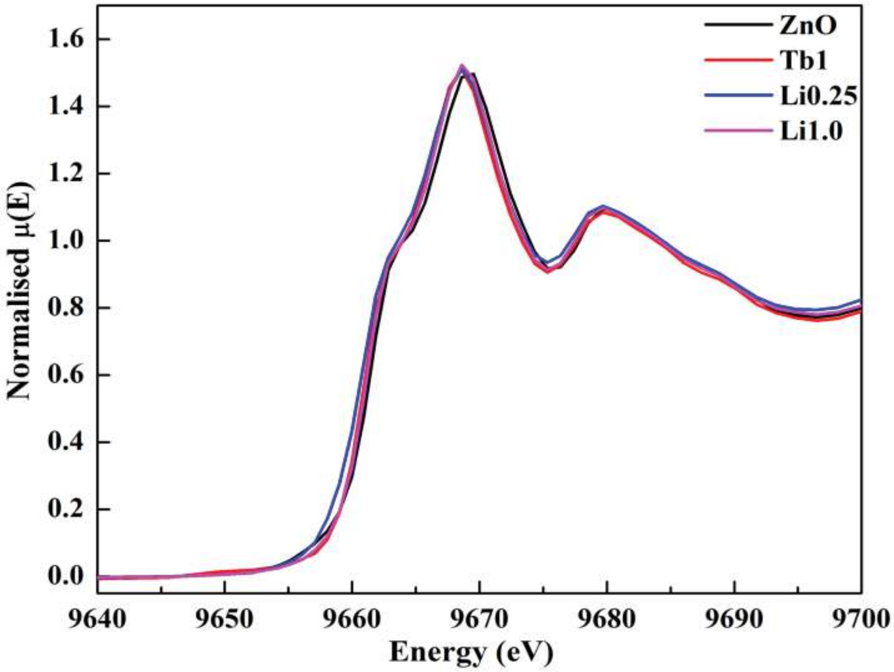

Figure 6.8: Normalised XANES spectra of Tb and Li co-doped ZnO measured at Zn K-edge.

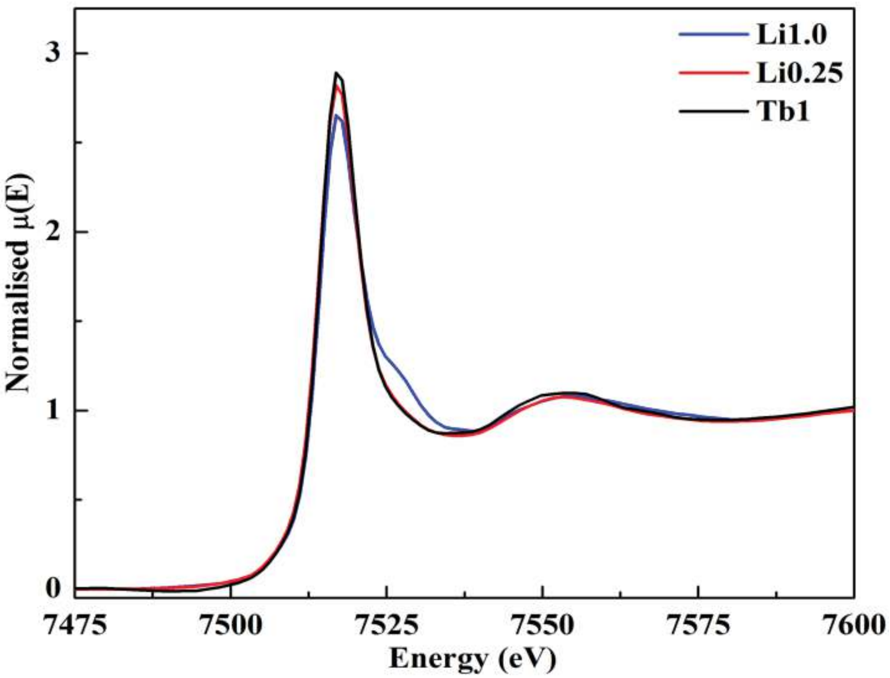

Figure 6.9: Normalised XANES spectra of Tb and Li co-doped ZnO measured at Tb L3 edge.

EXAFS Analysis

The normalized EXAFS spectra are shown in Figure6.10 and Figure 6.11 at Zn K-edge and Tb L3 edges respectively. In order to take care of the oscillations, we have converted the absorption spectra $\mu(E)$ to absorption function $\chi(E)$ using the relation as discussed in chapter 5. The wave number dependent absorption function $\chi(k)$ has been obtained from energy-dependent absorption function $\chi(E)$.

The Fourier transformed EXAFS spectra *($\chi(R)$* Vs *R*) are shown in Figure 6.12 at Zn K edge for (Tb, Li) co-doped samples. The theoretical spectra are generated from the structural parameters of ZnO obtained from the rietveld refinement of XRD data. The bond length (R) and disorder factor (σ^2), which is the representation of mean square displacement in the bond length, are kept as the fitting parameters during the fitting and the best fitting results are plotted in Figure 6.13. The first peak in ZnO at 1.5 Å is the contribution of four oxygen atoms at the distance of 1.97 Å and the second peak at 2.9 Å is the contribution of 12 Zn atoms at the distance of 3.21 Å. The bond length for Zn-O and Zn-Zn coordination shell is approximately same for all the samples. The marginal decrease in bond length of Zn-O or Zn-Zn may be to preserve the crystal structure. The small decrease in the bond length for Tb doped ZnO may be due to the dopant effect. The σ^2 is found to be decreasing from ZnO to Tb doped ZnO and it is further slightly decreased for Li0.25 and Li1.0 for Zn-O coordination shell. σ^2 for Zn-Zn coordination shell shows opposite trends. The increase in the σ^2 for Zn-Zn coordination shell is obvious as the larger size of Tb atoms for Tb doped ZnO. The incorporation different Li could not significantly affect the bond length and disorder.

The Fourier transforms EXAFS spectra at Tb L3 edge is shown in Figure 6.14 and the best fitting results are shown in Figure 6.15. Single coordination peak between 1-2.5 Å is obtained for all three samples. The first coordination peak has been observed in the range of 1-2.5 Å. The peaks at higher bond distances are very weak. This indicates highly disordered local structure around Tb sites, which will not give the significant second coordination peak. This can be attributed to ionic radius mismatch between Tb^{+3}(0.92Å) and Zn^{+2} (0.74Å) ions. The ionic radii difference results too much disorder in the lattice. This peak is fitted with single Tb-O coordination shell around 2.33Å. The coordination number, bond length (R) and the disorder factor (σ^2) are kept as the fitting parameters during the fitting and the best fitting results are plotted in Figure 6.15. The Tb-O bond length is decreased from Tb doped ZnO to Li0.25. However, it is increased for Li1.0. This decrease in the bond length can be understood as follows. The lattice constants indicate side length for a hexagonal wurtzite crystal. The distance between nearest atoms is represented by bond length. Typically, smaller bond lengths mean the electrons are more tightly bound to the atom. The result of APF shows that APF of Li0.25 in greater than Tb1 (Table 6.1) i.e. system is more closely packed and the distance between nearest atom decreases. This leads to decrease in bond length. The coordination number and σ^2 are showing the decreasing trend. The decrease in the coordination number may be attributed to the increase in the oxygen vacancy type defects near the dopant sites.

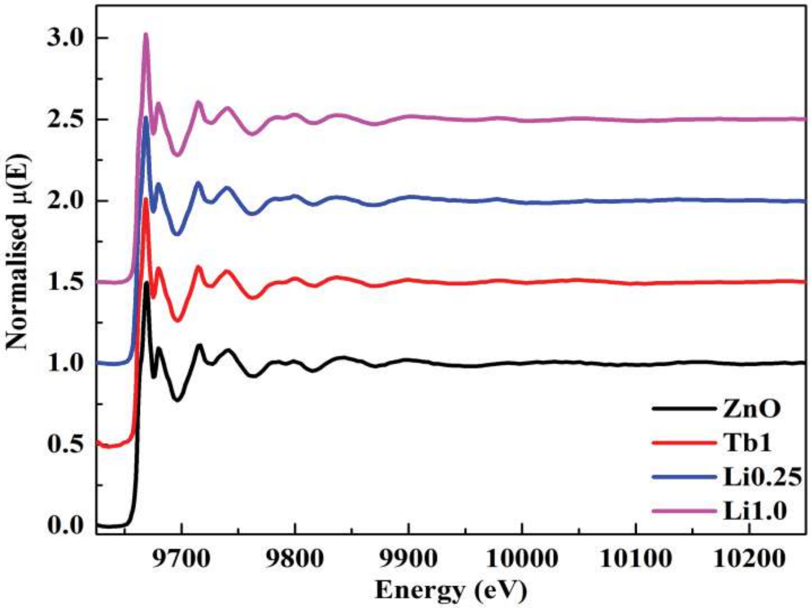

Figure 6.10: Normalised EXAFS spectra of Tb and Li co-doped ZnO measured at Zn K-edge.

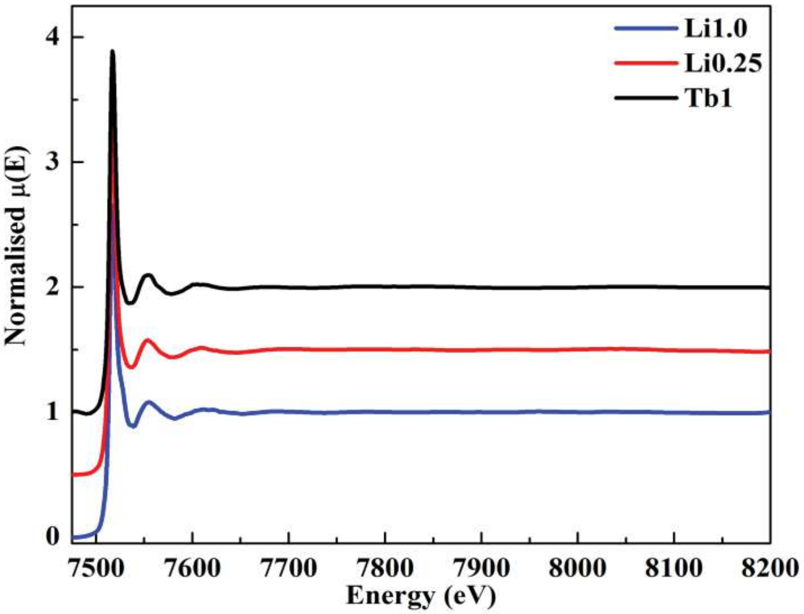

Figure 6.11: Normalised EXAFS spectra of Tb and Li co-doped ZnO measured at Tb L3-edge.

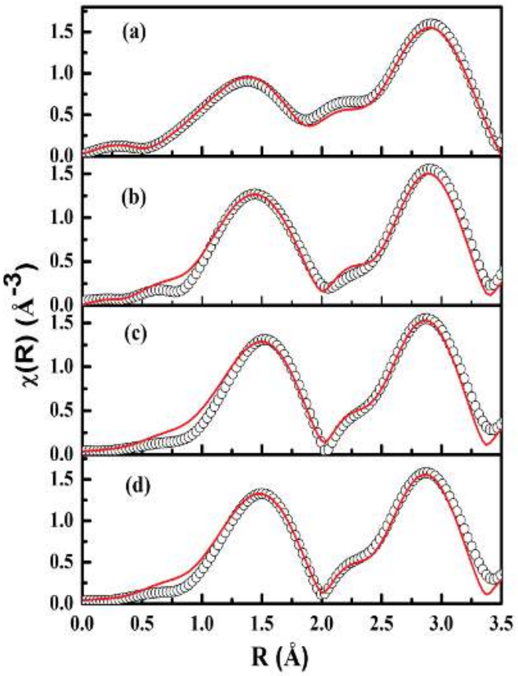

Figure 6.12: Fourier transformed EXAFS spectra of Tb and Li co-doped ZnO samples measured at Zn K-edge (Scatter points) along with the theoretical fit (Solid line): **(a)** ZnO, **(b)** Tb1 **(c)** Li 0.25 **(d)** Li1.0.

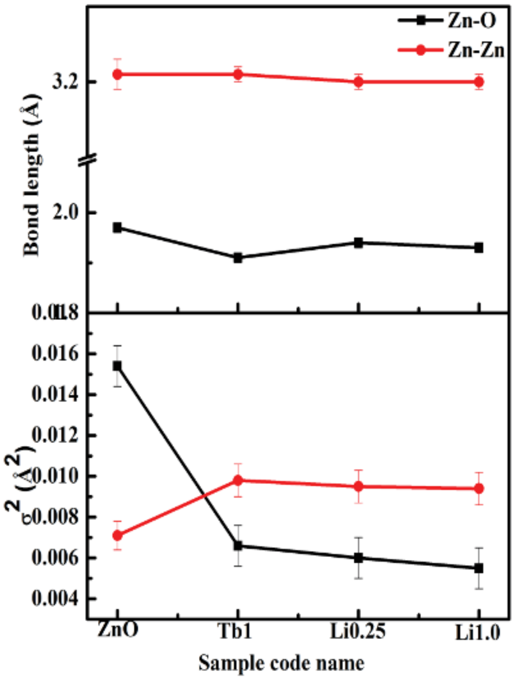

Figure 6.13: Variation of (top to bottom) bond length and disorder obtained from EXAFS fitting at Zn K edge.

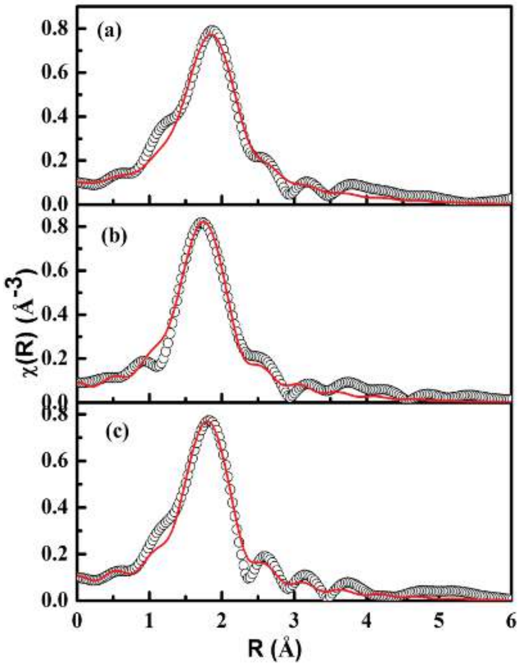

Figure 6.14: Fourier transformed EXAFS spectra of Tb and Li co-doped ZnO samples measured at Tb L3-edge (Scatter points) along with the theoretical fit (Solid line): (a) Tb1, (b) Li0.25 and (c) Li1.0.

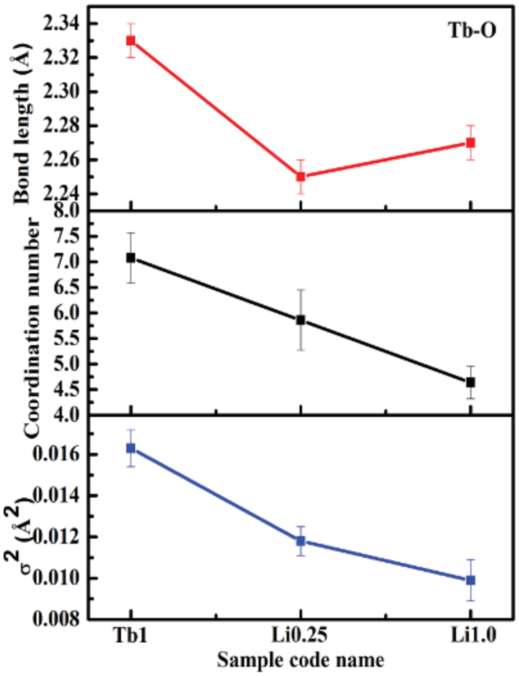

Figure 6.15: Variation of (top to bottom) bond length, coordination number and disorder obtained from EXAFS fitting at Tb L3 edge.

6.3.8 Absorption Study

The normalized absorption spectra of all the samples that measured in the range of 250nm-800nm are shown in Figure 6.16. The absorption spectra of all samples contain an intensive absorption in 250nm-400nm wavelength range. It has been observed that Tb doping results encroachment in the visible region up to 600nm. The incorporation of Li leads towards enhancement in the intensity of visible region absorption. The absorption edge shift towards higher wavelength may be attributed to Tb doping. In the case of Tb ions, 4f-4f electron transition makes a substantial contribution to visible region absorption. The absorption edge shift in Tb-doped ZnO has also been reported by authors [193]. In best of our knowledge, encroachment in the visible region up to 600nm with Tb, Li co-doped ZnO nanoparticles has not been reported earlier. The visible region encroachment in considered sample can be attributed to surface effect and change in particle size. The formation of defect levels in between conduction band and valance band are also responsible for visible region absorption. The incorporation of Li at substitutional position promotes the formation of shallow donor level, which results shift of absorption edge towards higher wavelength. The band gap of all samples has been calculated with the help of Tauc relation (Equation 3.2). Tauc plot of pure ZnO and doped ZnO are shown in Figure 6.17(a-e). The band gap of the sample has been estimated using extrapolation of a linear part that meets the abscissa of Tauc plot. The variation in the band gap with different doping has been shown in Figure 6.17(f). It has been found that band gap decreases by Tb doping in ZnO nanoparticles. The band gap decrease can be attributed to the formation of donor level by Tb^{+3} ions below the conduction band. *Hastir et al.* also observed a decrease in band gap due to Tb doping in ZnO nanoparticles [178]. A small increase in band gap has been obtained due to Li co-doping but band gap is still less than the band gap of ZnO. The phenomenon can be explained with the help of

Burstein-Moss effect[194]. The increase in band gap may be due to the presence of Li ions in the host. The Tb^{+3}ions have been already occupied at donor level below the conduction band. The Li co-doping in Tb doped ZnO causes an increase in electron concentration, thus the apparent band gap is slightly increased.

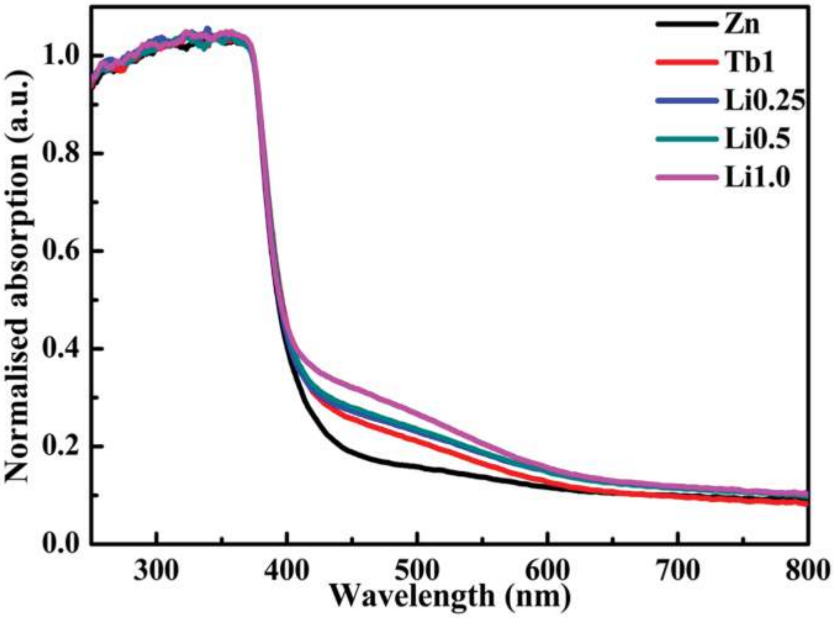

Figure 6.16: Absorption spectra of pure and doped zinc oxide nanoparticles.

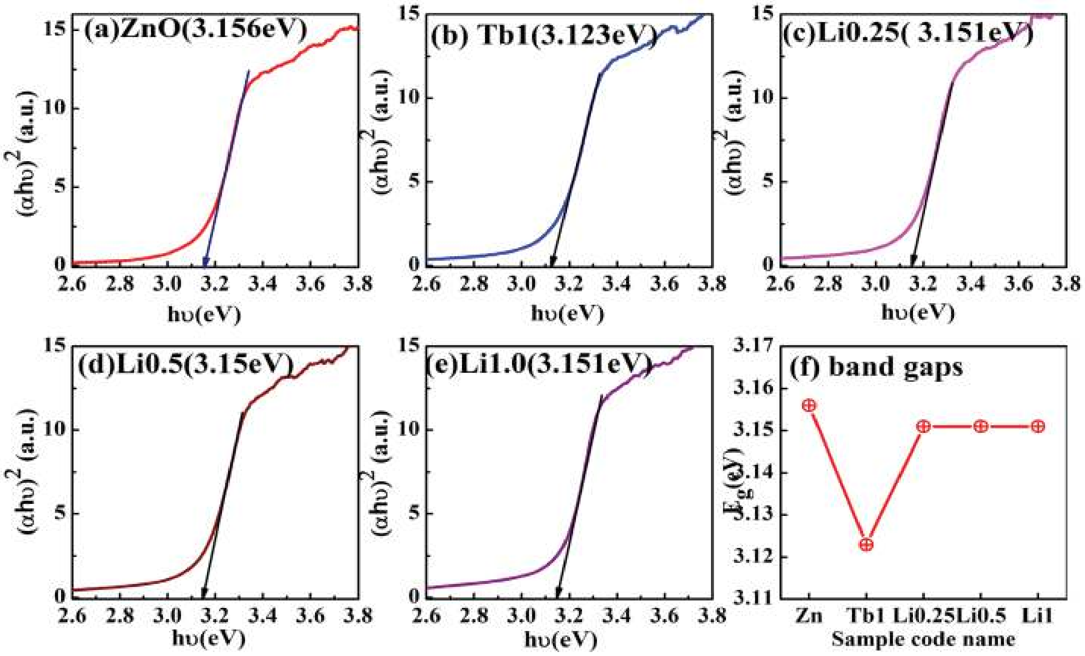

Figure 6.17: Tauc plot of **(a)** ZnO **(b)** Tb1 **(c)** Li0.25 **(d)** Li0.5 **(e)** Li1.0 **(f)** variation of energy band gap with composition.

6.3.9 Photoluminescence Study

The room temperature photoluminescence spectra of pure and doped zinc oxide samples recorded at an excitation wavelength 320nm are shown in Figure 6.18(a). Zinc oxide exhibits a wide emission in the visible region with most prominent peak in violet color. The deconvoluted spectra of pure ZnO are shown in Figure 6.18(b). The incorporation of Tb and Li could not significantly affect the spectrum nature and most intense peak position of host. A small decrease in intensity has been observed due to Li co-doping. The deconvoluted spectra of pure ZnO exhibit five peaks at 395nm, 433nm, 465nm, 484nm and 569nm. The observed emission can be divided in to two parts. (i) Emission in 350nm-400nm range (NBE) and (ii) emission in 400nm-650nm range. The peak arises around 398 nm can be assigned as near band edge emission (NBE). The recombination of an excited electron localized below the conduction band with holes in the valence band results the NBE emission [142]. The peaks observed in the range of 400nm-600nm are related to deep band emission, which is originated due to defect in the system, such as Zn interstitials, oxygen interstitials, Zn vacancy and oxygen vacancy [178]. The presence of Zn interstitial is responsible for peaks in a violet region around 434nm. Since shallow donor levels have long lifetime than conduction band. Therefore, electron relaxes in this level and then makes a transition to the valence band. The violet region emission arises due to electron transition from shallow donor level (Zn_i) to valence band. The blue emission near 465nm and 484nm are originated due to the defect related positively charge Zn vacancies [112]. The green emission observed around 569nm can be accredited to the presence of singly ionized oxygen vacancies.

In order to observe the visible emission of Tb, we have recorded the excitation spectra (λ_{emi}=540nm) of Tb (1%) doped ZnO nanoparticles (shown in Figure 6.19) the excitation spectra clearly indicates that 397nm wavelength is most suitable excitation wavelength. The observed excitation peak can be attributed to the *f-f* transition of Tb^{+3} ions [152]. The photoluminescence emission spectra of Tb and Li co-doped ZnO excited with 397nm are shown in Figure 6.20. The Tb^{+3} related peak detected at 539nm can be ascribed as the $^5D_4 \rightarrow {}^7F_5$ transition. We found that intensity of Tb^{+3} related peak increases with Li concentration up to Li (0.5%). The presence of Li ions plays an important role in luminescence enhancement of rare earth ions in different host materials. In our case, the small ionic radius of Li ions supports its incorporation in host lattice without disturbing the Zn^{+2} site of the lattice structure. When small amount of Li is co-doped in Tb doped ZnO, Li takes interstitial positions. The incorporation of Li at interstitial position enhances the transition probability of Tb^{+3} related peak. The charge compensation phenomenon required only small concentration of Li ions. The increase in Li concentration causes substitution of Li at Zn^{+2} sites of ZnO crystal structure. The Li substitutional produces negative charge as well as increase oxygen vacancy for charge neutralization in the host lattice. The XPS results support the enhancement in oxygen vacancies and confirm the presence of Li interstitials and Li substitutional. The higher amount of Li concentration does not favors luminescent related to rare earth and causes decrease in intensity due to luminescence quenching [152]. The study suggests that ZnO: Tb(1%):Li(0.5%) is the best suitable combination for enhanced luminescence.

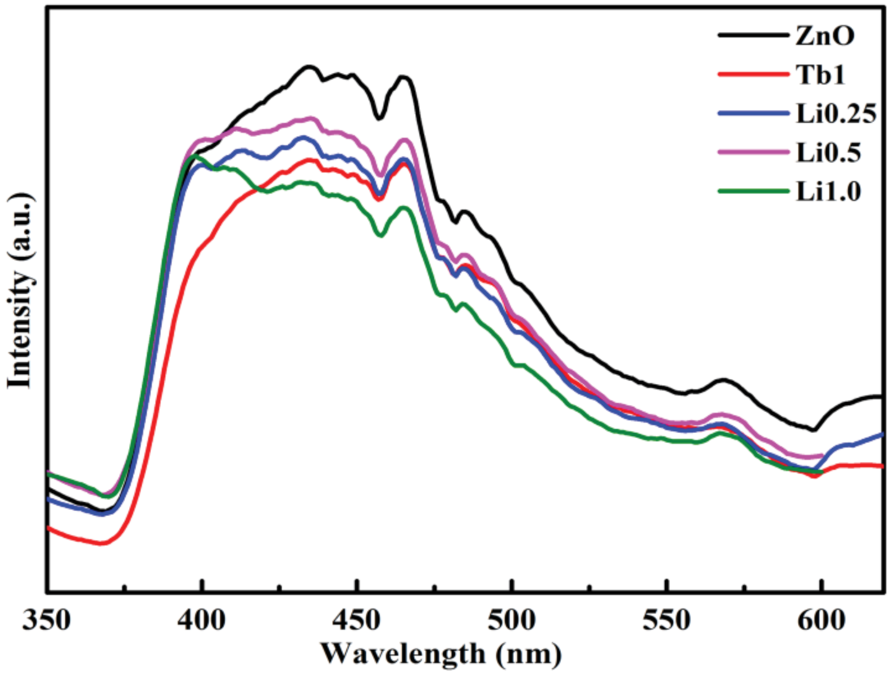

Figure 6.18(a): Photoluminescence emission spectra of pure and doped zinc oxide at λ_{ex}=320 nm

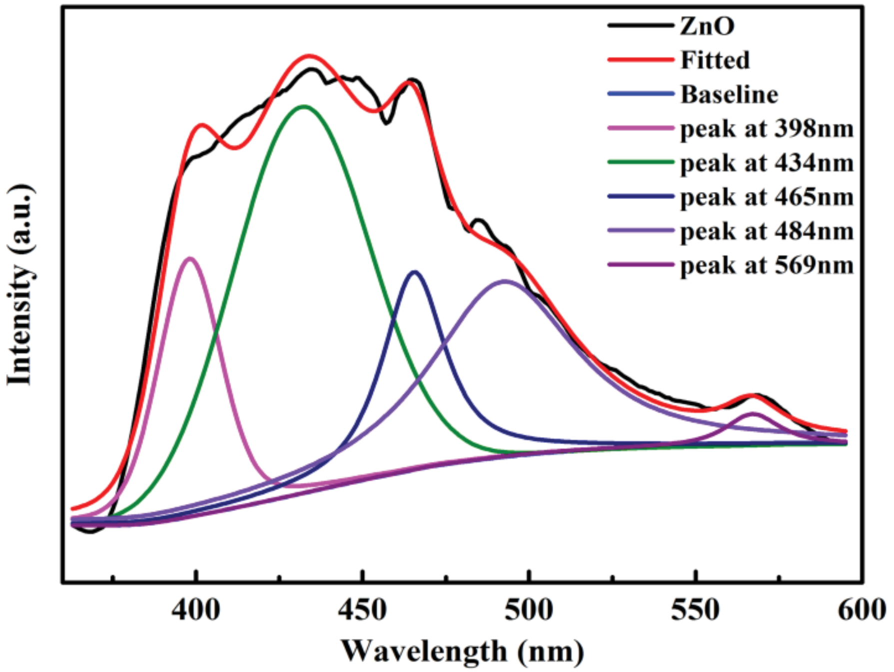

Figure 6.18(b): Deconvoluted Photoluminescence emission spectra of pure zinc oxide at λ_{ex}=320 nm

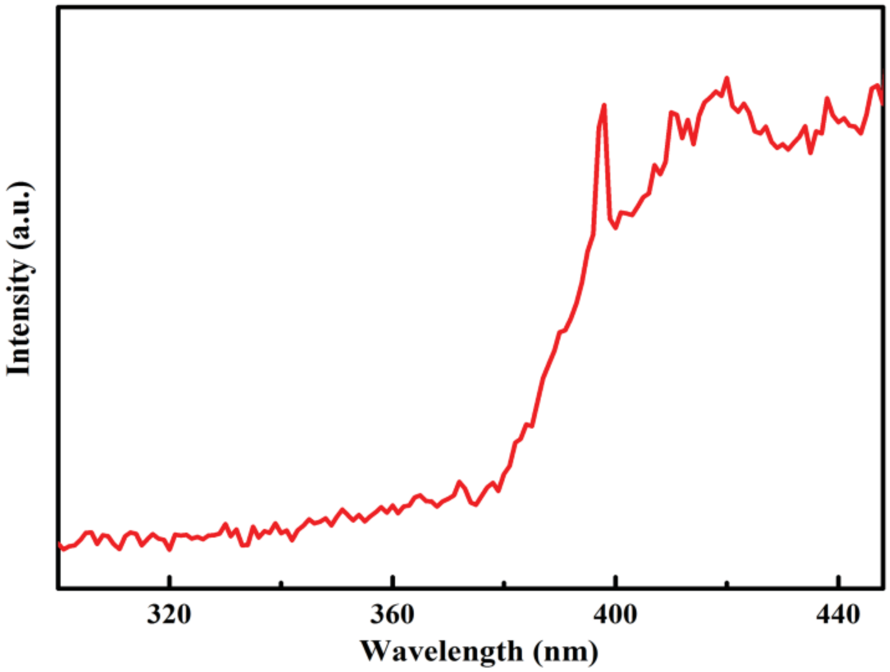

Figure 6.19: Photoluminescence excitation spectra of Tb doped ZnO at λ_{em}=540 nm.

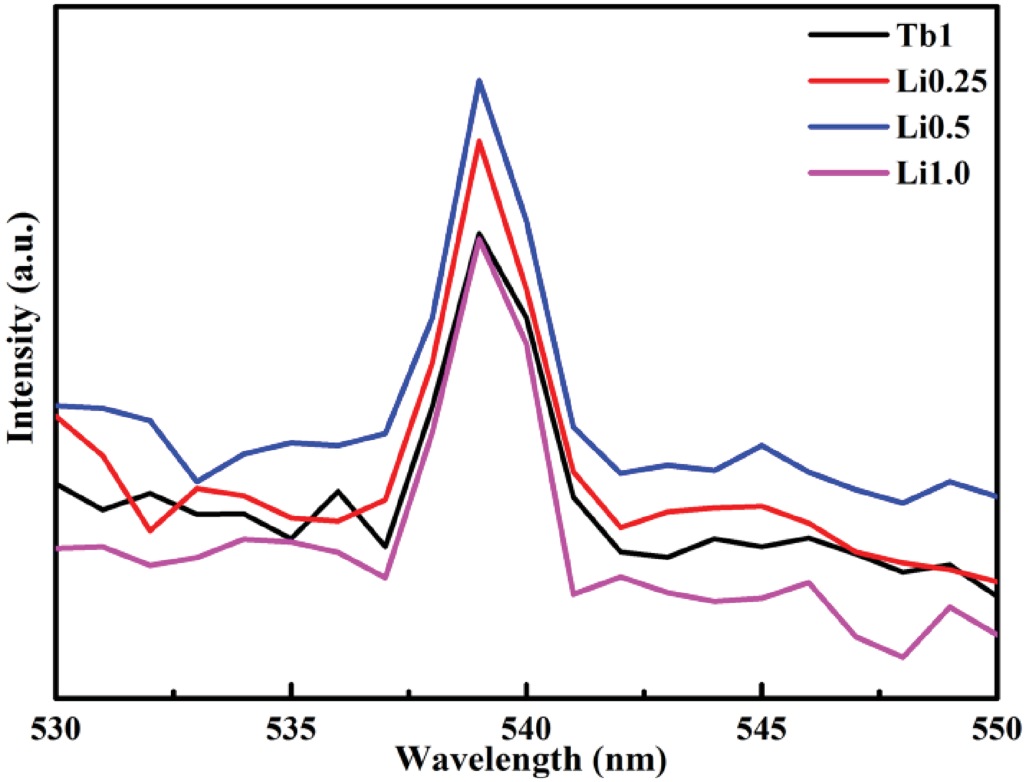

Figure 6.20: Photoluminescence emission spectra of pure and doped ZnO at λ_{ex}=397 nm.

6.3.10 Magnetic Properties

The magnetization curve recorded at room temperature is shown in Figure 6.21. It can be pointed that pure ZnO shows room temperature ferromagnetic behavior with the diamagnetic contribution at high magnetic field, while Tb and (Tb, Li) co-doped ZnO shows weak ferromagnetic contribution due to host. The pure ZnO are diamagnetic without any impurity or defect state. The high orbital moment of the 4f electron in Tb^{+3} ions leads to magnetic moment 9 μB per Tb atom [195]. Terbium is naturally paramagnetic at room temperature. The Tb doping in ZnO decreases the ferromagnetic property of ZnO. The close inspection near the origin for ZnO and doped ZnO is shown in Figure 6.22(a) and 6.22(b) respectively. It indicates that pure ZnO exhibit ferromagnetic property. The close inspection near origin in Tb doped ZnO [Figure 6.22(b)] ascertain that Tb doped ZnO have weak ferromagnetic behavior. The observed weak ferromagnetic contribution in Tb doped ZnO may be due to host ZnO. The experimental results on RTFM of ZnO are quite controversial. The studied shows that ZnO behaves like diamagnetic or ferromagnetic depend on preparation condition. Since ferromagnetic response depends on defects such as Zn vacancies and oxygen vacancies, so it's difficult to reproduce the pure ZnO with same magnetic moment even with same preparation method. The ferromagnetic behaviour in Tb-doped ZnO thin film has been reported by *Zou et al.*[149]. They explained that grain boundary of the surface state is responsible for ferromagnetic ordering. *Bandhopadyay et al.* observed paramagnetic to ferromagnetic transition in Tb-doped ZnO at low temperature [196]. It has been reported that samples are paramagnetic at room temperature. Their observed results indicate that magnetic moments of Tb^{+3} ions are not perfectly aligned even at temperature 5K and applied magnetic field 5T. *Lotely et al.* claimed FM in Tb-doped ZnO due to induced defect [195]. In our results, we found small values of H_c and M_r in all the samples. Pure

ZnO shows diamagnetic behaviour, but H_c (50.12Oe) and M_r (6.56 x 10^{-4}emu/g) values indicate that ferromagnetic contribution is also present in the sample. A very small hysteresis is observed with Tb doping [as shown in Figure 6.22(b)], which might be due to the contribution present in the host (H_c=21.55Oe, M_r=2.42 x 10^{-4}emu/g). The H_c and M_r values of all samples are listed in Table 6.2. The magnetic behaviour of doped ZnO is affected by distribution, the distance between dopant ions and oxygen vacancy. The first principle calculation of rare earth (Tb, Eu, Dy etc.) doped ZnO suggest that large separation between rare earth ions is responsible for paramagnetic behaviour in rare earth doped ZnO [197]. Two different configurations were used for theoretical prediction of magnetic properties in rare earth doped ZnO. In the near configuration, two dopant atoms were considered as the nearest neighbour separated by one oxygen atom. In case of far configuration, the dopant ions were at a large distance separated by the chain of -O-Zn-O- atoms. Therefore, first principle calculation ascertains that magnetic behaviour depends on distribution and the distance between dopant ions i.e. concentration of dopant ions. The magnetic behaviour depends on magnetic moments due to Tb^{+3} ions. In our system, the doping concentration is very small (Tb 1%). Since the system is very dilute, the effective distance between Tb^{+3} ions within the particle or inter-particle is very large. Therefore, the interaction between Tb^{+3} ions is very low which in effect leads to weak hysteresis in the system. The observed weak ferromagnetism at room temperature can also be explained with the help of electron configuration of Tb^{+3} ions. Iron is well known for ferromagnetism. The comparison between Tb and Fe on the basis of electronic configuration indicates that 4f shell of Tb ions is well protected by 5d and 6s shell. This affects the exchange interaction among the electrons. In the case of Fe, the 3d shell can be considered as the outermost shell. This facilitates the interaction between neighbouring atoms.

The FM in Li-doped ZnO has been reported by different authors[198], which is due to defect in the system. The Li ions are non-magnetic. They enhance the FM by stabilizing cation vacancies (which has a local magnetic moment) as well as introduce holes in the system. This mechanism is more suitable for high Li doping concentration. In our case, when a small amount of Li has been used as charge compensator, it occupies an interstitial position. The increase in the doping concentration (Li1%) causes substitution of Li ions at the Zn^{+2} site of ZnO crystal structure and introduce holes in the system. *Lader et al.* reported that behaviour of Li as an acceptor or donor depends on its position [199]. The presence of Li at interstitial and substitutional position indicates acceptor and donor behaviour respectively. The XPS analysis confirms the presence of Li in the Li1.0 sample. It was found that Zn interstitials and vacancies are also responsible for paramagnetic behaviour [200]. The variation in doping concentration of Li could not make a significant change in the magnetic behaviour of Tb-doped ZnO. The Tb and Li co-doped samples exhibit small values of H_c and M_r (For Li1.0; H_c=21.36 Oe, M_r=1.64 x 10^{-4} emu/g). The ZFC plot of all samples is shown in Figure 6.23. The inset shows the susceptibility curve for pure ZnO. We can say that susceptibility values decrease with increase in temperature. In light of observed results and above discussion, we can conclude the magnetic behaviour in our sample. The structural analysis (XRD, FTIR and Raman), elemental analysis (EDS), local structure investigation by EXAFS authenticates that samples do not have any impurity phase within the detection limit of instruments. A small lattice distortion has been obtained due to the incorporation of Tb and Li atoms. The XPS analysis ascertained the oxidation states of (Tb, Zn, Li, and O), and presence of Li in Li1.0 sample. Thus the impurity phase is not responsible for magnetic behaviour in the present case. Pure ZnO shows diamagnetic behaviour with some ferromagnetic contribution. The observed ferromagnetism in pure ZnO can be attributed to defects (such as Zn vacancies and oxygen vacancies) in the sample. Tb doped ZnO shows weak ferromagnetic behaviour. The observed weak ferromagnetic behaviour is due to a large effective distance between Tb ions and protection of 4f electron by 5d and 6s shell. The weak ferromagnetic contribution may also be due to defects in the host ZnO. The incorporation of Li causes stabilization of cation vacancies, which support the magnetic behaviour of terbium in Tb, Li co-doped ZnO samples. Therefore, observed magnetic behaviour in our sample may be due to the combined effect of dopant (Tb) and defect in the system.

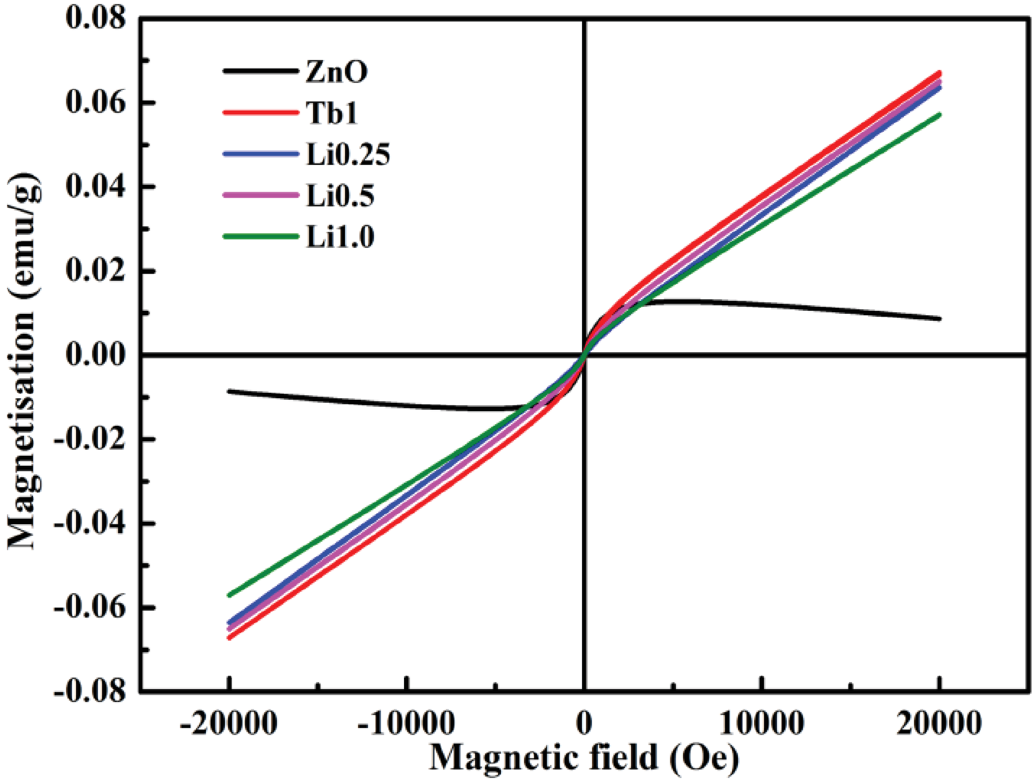

Figure 6.21: M-H curve of pure and doped ZnO nanoparticles at 300 K.

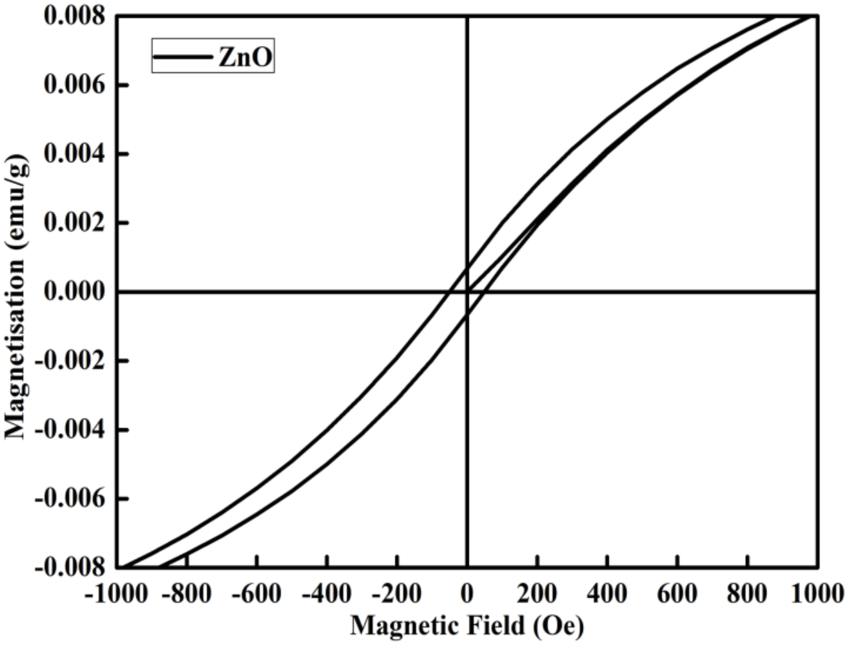

Figure 6.22(a): M-H curve of pure ZnO nanoparticles at 300 K.

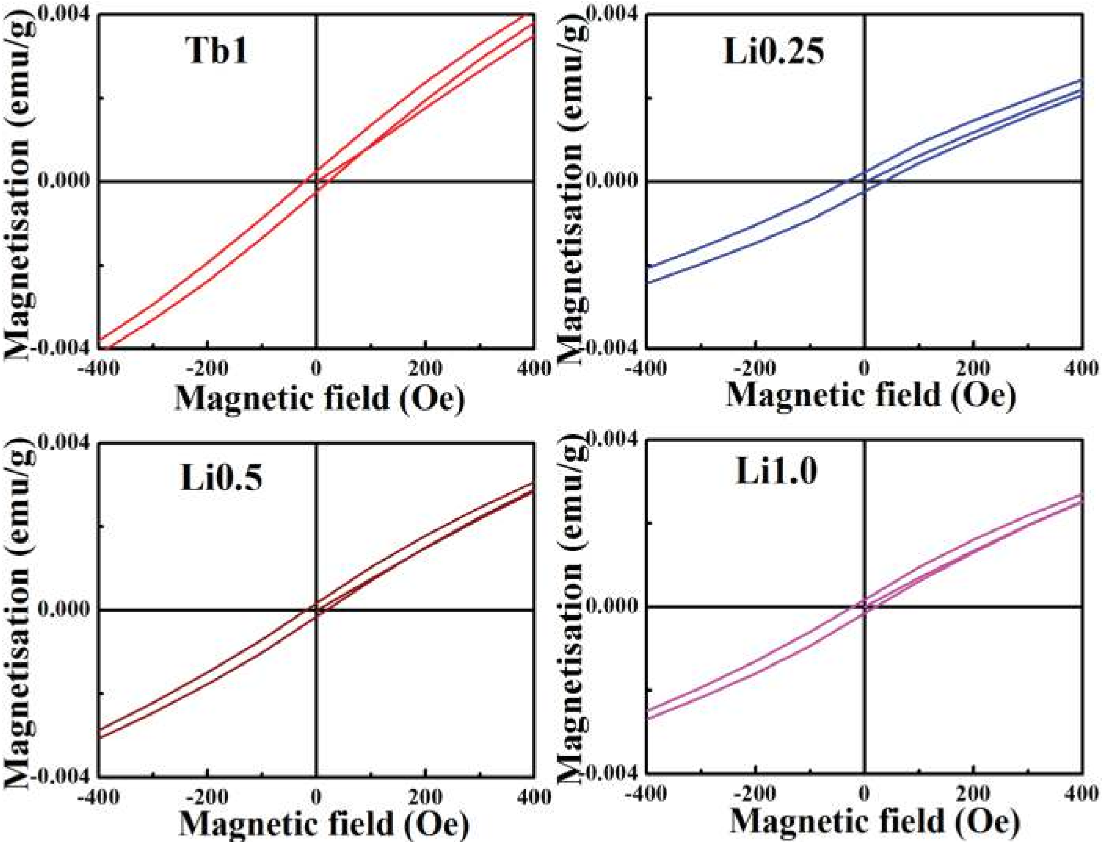

Figure 6.22(b): M-H curve of doped ZnO nanoparticles near origin.

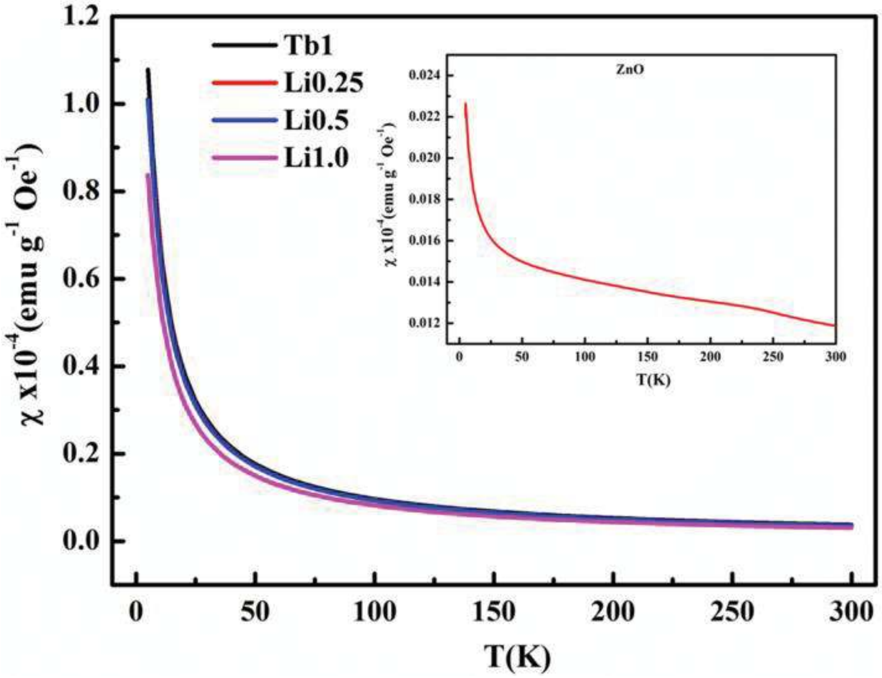

Figure 6.23: Susceptibility curve of pure and doped ZnO nanoparticles.

Table 6.2: The H_c, and M_r values of pure and doped ZnO nanoparticles

Sample name	H_c (Oe)	M_r (emu/g)x 10^{-4}
ZnO	50.12	6.56
Tb1	21.55	2.42
Li0.25	33.86	2.83
Li0.5	18.28	1.60
Li1.0	21.36	1.64

6.4. CONCLUSION

The present study explores the effect of Tb and Li co-doping on structural, optical and magnetic properties of zinc oxide. The thermal study suggests the appropriate temperature for crystallization of sample. The structural properties have been investigated with the help of XRD, Raman, FTIR and XAS characterization. The structural analysis ascertains that all samples exhibit wurtzite crystal structure without any traces of impurity phase. The lattice parameters obtained from Rietveld refinement of XRD shows small variation due to dopant. In order to shed more light on the local structure, we carried out XAS analysis. The results of EXAFS and XANES ensure a clear signature of terbium substitution and +3 oxidation state in the samples. The oxidation state measured by XPS is fully consistent with XANES measurement. The observed bond length variation and XPS study ascertain the presence of Li in the lattice. We found encroachment in the visible region absorption up to 600nm for Li1.0. It has been observed that band gap decreases due to Tb doping in ZnO nanoparticles. The small increase in the band gap has been observed due to Li co-doping. We have tuned Li co-doping concentration to find suitable amount required to enhance the luminescence of Tb related peak. We found Tb^{+3} related peak at 539nm and enhancement in this peak occurs due to Li co-doping. The maximum intensity has been recorded for Li0.5 sample. The magnetic property of this system has not been reported earlier. The magnetic property of ZnO has been changed due to doping of Tb and Li. Pure ZnO shows ferromagnetic behavior, while Tb-doped ZnO shows weak ferromagnetic behaviour. In this article, we report luminescence enhancement in Tb doped ZnO by Li co-doping. A more intense peak can be observed by changing Tb concentration and using the same concept of charge compensation.